Modeling Solvent Evaporation During the Manufacture of Controlled Drug Release Coatings and the Impact on Release Kinetics

Chang-Soo Kim[1], David M. Saylor[1], Martin K. McDermott[1], Dinesh V. Patwardhan[1], and James A. Warren[2]

[1] *Food and Drug Administration, Center for Devices and Radiological Health, Office of Science and Engineering Laboratories, Silver Spring, MD 20903*

[2] *National Institute of Standards and Technology, Metallurgy Division, Materials Science and Engineering Laboratories, Gaithersburg, MD 20899*

Abstract

To improve functionality and performance, controlled drug release coatings comprised of drug and polymer are integrated with traditional medical devices, e.g. drug eluting stents. Depending on manufacturing conditions, these coatings can exhibit complex microstructures. Previously, we developed a thermodynamically consistent model for microstructure evolution in these systems to establish relationships between process variables, microstructure, and the subsequent release kinetics. Calculations based on the model were, in general, consistent with experimental findings. However, because of assumptions regarding the evaporation of solvent during fabrication, the model was unable to capture variations through the coating thickness that are observed experimentally. Here, we introduce a straightforward method to incorporate solvent evaporation explicitly into the model. Calculations are used to probe the impact of solvent evaporation rate and drug loading on the microstructure that forms during manufacturing and subsequent drug release kinetics. We find that the predicted

structures and release kinetics are consistent with experimental observations. Further, the calculations demonstrate that solvent evaporation rate can be as critical to device performance as the amount of drug within the coating. For example, changes of a factor of five in the amount of drug released were observed by modifying the rate of solvent evaporation during manufacturing.

Keywords: controlled drug release, drug delivery, modeling, microstructure, stent, composite, confocal microscopy

1 Introduction

In recent years, controlled release coatings, comprised of drug-polymer composites, have been integrated with medical devices, improving device functionality and performance. Most notably, drug eluting stents (DES) have demonstrated a significant reduction in the rate of restenosis after angioplasty compared to bare metal stents [1–3]. Fabrication of drug eluting coatings typically begins with an initially homogeneous solution of drug, polymer, and solvent. The coating is then cast or sprayed onto the surface of the device; the solvent evaporates, leaving behind an nearly pure composite of drug and polymer. These composite structures typically exhibit phase-separated morphologies (drug-rich regions in a polymer matrix) , which depend on the physico-chemical properties of the materials, solution composition, and environmental conditions. The morphology that evolves during fabrication will, in turn, have a substantial impact on the kinetics of drug release [4–7].

Previously, we developed a thermodynamically consistent diffuse-interface theory to predict microstructure evolution of controlled release coatings during both manufacturing and drug release, enabling the relationships between processing, microstructure, and release to be evaluated for any material system over a wide range of environmental conditions based only on a small set of well-defined and measurable thermodynamic and kinetic material properties [8]. Calculations based on the theory have been used to explore the effects of drug loading, evaporation rate, drug-polymer phobicity, and release media (polymer-soluble and polymer-insoluble) on microstructure formation and drug release [9]. While the predictions were generally consistent with existing experimental data, the model did not treat evaporation

during coating fabrication explicitly. Instead, the evolution time was used to approximate the impact of evaporation rate, which assumes that solvent is removed homogenously throughout the system. By making this approximation, the model was not able to capture structural gradients that may develop due to inhomogeneous removal of solvent during evaporation (e.g. the formation of layered structures). However, as illustrated in Fig. 1, controlled release coatings do, in fact, develop gradients through the thickness of the coating. *Thus, the objective of the work described here is to extend the previous theory to explicitly incorporate the effects of evaporation, enabling the model to not only capture the potential development of microstructural gradients, but also the impact of these gradients on drug release.*

While a full treatment of evaporation within the diffuse interface framework is analytically straightforward, it would add substantial complexity and make predictions based on the model intractable. Therefore, we have developed a straightforward method to integrate evaporation into the previous model through the introduction of a unique boundary condition and mesh redistribution algorithm. The boundary condition captures the essential physics of evaporation without requiring a complete physico-chemical description of the system constituents in the gas phase. Here, we apply the new model to assess the impact of both evaporation rate and drug loading on structure formation and drug release behavior, and compare and contrast the results with those derived from the previous model. We note that while the focus of this manuscript is on the behavior of controlled drug release coatings, the approach outlined can be applied to simplify models of processes, such as evaporation, where one or more of the constituents is systematically removed from the system.

In this manuscript, we apply the new, more robust model to explore the relationships between

process variables, microstructure, and release kinetics in controlled drug release systems and compare the results with previous predictions. In the following section, we provide a brief overview of the existing model, along with a description of the new, explicit treatment of evaporation. Further, the specific material properties and simulation parameters are given. We then illustrate the outcome of the calculations, followed by a discussion of the results, which includes a comparison to predictions based on the previous model. Finally, we provide a brief overview in the Summary section.

2 Materials and Methods

The diffuse-interface theory developed to predict microstructure evolution and drug release kinetics in controlled drug delivery systems is based on two well-known continuum equations, the Cahn-Hilliard [10,11] and Allen-Cahn [12] equations. These methods enable predictions of microstructure evolution to be made for any arbitrary system based a small-set of well-defined, measurable material quantities. In contrast, previous theoretical efforts in controlled drug release, reviewed recently in [13], focused primarily on empirical models [14,15] and mean-field approaches [4,16] specific to a particular class of material systems. Furthermore, although statistical, Monte Carlo methods have been successfully employed to incorporate the effect of microstructure explicitly [17,18], they do not account for the effect of processing on the structure. We note that the diffuse interface theory for microstructure evolution in controlled release systems, which did not explicitly include solvent evaporation during processing, has already been described in detail [8,9]; however, for completeness we provide

a brief overview in the following section. The overview of our previous model is followed by a description of the explicit evaporation scheme adopted in the current model. Finally, materials specific parameters and simulation conditions are detailed.

2.1 The Model

The thermodynamically consistent diffuse interface model for microstructure evolution in controlled release systems consists of three-components, drug (d), polymer (p), and solvent (s), which are specified by their respective volume fractions, ϕ_i, where i is equal to d, p, and s. Further, the components can assume both crystalline and amorphous states, and an order parameter η that varies between zero (amorphous) and one (crystalline) is used to specify the local degree of crystallinity. Based on these parameters, we can express the time evolution of the system in terms of three dimensionless partial differential equations [8,9]:

$$\frac{\widetilde{\partial \phi_d}}{\partial t} = \widetilde{\nabla} \cdot \frac{D_d(\phi_i,\eta)}{D^0 f''_{ideal}(\phi_d)} \widetilde{\nabla} \left[\frac{\partial f(\phi_i,\eta)}{\partial \phi_d} - \frac{\partial f(\phi_i,\eta)}{\partial \phi_s} - \frac{\epsilon^2}{\lambda^2} \left(2\widetilde{\nabla}^2 \phi_d + \widetilde{\nabla}^2 \phi_p \right) \right] + \xi_d, \tag{1}$$

$$\frac{\widetilde{\partial \phi_p}}{\partial t} = \widetilde{\nabla} \cdot \frac{D_p(\phi_i,\eta)}{D^0 f''_{ideal}(\phi_p)} \widetilde{\nabla} \left[\frac{\partial f(\phi_i,\eta)}{\partial \phi_p} - \frac{\partial f(\phi_i,\eta)}{\partial \phi_s} - \frac{\epsilon^2}{\lambda^2} \left(2\widetilde{\nabla}^2 \phi_p + \widetilde{\nabla}^2 \phi_d \right) \right] + \xi_p, \tag{2}$$

$$\frac{\widetilde{\partial \eta}}{\partial t} = -\frac{M_\eta(\phi_i)\lambda^2}{D^0} \left[\frac{\partial f(\phi_i,\eta)}{\partial \eta} - \frac{\alpha^2}{\lambda^2} \widetilde{\nabla}^2 \eta \right] + \xi_\eta, \tag{3}$$

with characteristic length and time scales, λ and λ^2/D^0, respectively, where D^0 is a characteristic diffusivity and quantities with tildes are dimensionless. Note that $\phi_d + \phi_p + \phi_s = 1$, and therefore, only two equations are required to describe the evolution of the composition fields, ϕ_i. Here, we have arbitrarily elected to eliminate the equation for the rate of change

of ϕ_s. Also, ξ_i represent the appropriate Langevin noise terms modeling random fluctuations [19]. The remaining quantities in Eqns. 1-3 arise due to bulk thermodynamic, interfacial, and kinetic contributions and are described in detail in the following paragraphs.

The bulk thermodynamic contributions to microstructure evolution are encompassed in the quantity $f(\phi_i, \eta)$, the homogenous free energy density, is based on the well-known Flory-Huggins model [20,21] and given by :

$$f(\phi_i, \eta) = f^a(\phi_i) + p(\eta)\Delta f(\phi_i) + \sum_i^3 w_i \phi_i g(\eta) + \beta \sum_i^3 \frac{1}{\phi_i}, \tag{4}$$

with:

$$f^a(\phi_i) = RT \sum_i^3 \frac{\phi_i}{V_i^m} \ln \phi_i + \frac{RT}{V^s} \sum_i^3 \sum_{j,j>i}^3 \chi_{ij}^a \phi_i \phi_j,$$

$$\Delta f(\phi_i) = \sum_i^3 \phi_i \frac{L_i(T - T_i^m)}{T_i^m} + \frac{RT}{V^s} \sum_i^3 \sum_{j,j>i}^3 \Delta\chi_{ij} \phi_i \phi_j,$$

$$w_i = \frac{3\gamma_i T}{\sqrt{2}\delta_i T_i^m}, \qquad g(\eta) = \eta^2(1-\eta)^2, \qquad p(\eta) = \eta^3(10 - 15\eta + 6\eta^2).$$

In Eqn. 4, R and T are the gas constant and prescribed temperature, respectively, V_i^m are the molecular volumes of the individual components, and V^s, the volume of an individual site on a hypothetical molecular lattice, is taken to be the minimum of V_i^m. Also, χ_{ij}^a are the interaction parameters (*i.e.* the relative chemical phobicity) in the amorphous state related to the enthalpy of mixing, while $\Delta\chi_{ij} = \chi_{ij}^c - \chi_{ij}^a$, *i.e.* the difference in the interaction parameters in the crystalline and amorphous states. The other quantities in Eqn. 4 reflect the thermodynamic properties of the pure materials. These include: the energies and thicknesses of interfaces between crystalline and amorphous regions, γ_i and δ_i, respectively, and the latent

heats of fusion, L_i and the melting (crystallization) temperatures, T_i^m. The final quantity, β, represents a weight factor for the final term in Eqn. 4, which is a modification to the free energy introduced to improve numerical efficiency, while not substantially altering the rate of structural evolution or the geometry of the features that evolve [8].

The fourth order terms in Eqns. 1 and 2 and the second order term in Eqn. 3 derive from corrections to the system free energy to account for the presence of interfaces. These terms contain coefficients, ϵ and α, which are related to the properties of interfaces within the system. For example, α^2 gives rise to interfaces between crystalline and amorphous phases and is specified by the properties of interfaces between the pure components [8]:

$$\alpha^2 = \frac{6\sqrt{2}\gamma_i\delta_i T}{T_i^m}. \tag{5}$$

Similarly, ϵ underlies interfaces between phases of different composition and non-trivially specifies the relationship between χ_{ij}^k, γ_{ij}^k, and δ_{ij}^k, where γ_{ij}^k, and δ_{ij}^k are the energy and thickness, respectively, of these interfaces [8,9].

The remaining unspecified quantities in Eqns. 1-3 are kinetic contributions that include the diffusivities $D_i(\phi_i, \eta)$ of the components. Here, we approximate the phase and composition dependence of the diffusivity of the relatively large molecular species in solvent [22–24] with

the following function:

$$\frac{D_i(\phi_i,\eta)}{D^0[1-p(\eta)]} = \begin{cases} 10^{(-A_i(0.2-\phi_s))} & \phi_s \leq 0.20 \\ 1 & \phi_s > 0.20, \end{cases} \tag{6}$$

where A_i captures the decrease in diffusivity when the solvent concentration falls below 20 % and $[1-p(\eta)]$ models the dramatic reduction that occurs in crystalline regions compared to those that are amorphous. The mobility of interfaces between crystalline and amorphous material $M_\eta(\phi_i)$ is specified assuming that the rate molecules join a growing crystal is controlled by diffusive jumps:

$$\frac{M_\eta(\phi_i)\alpha^2}{D^0} = \phi_d \frac{D_d(\phi_i)}{D^0} + \phi_p \frac{D_p(\phi_i)}{D^0} + \phi_s, \tag{7}$$

and finally, $f''_{ideal}(\phi_i)$, also known as the ideal solution thermodynamic factor, is given by $RT(1/\phi_i V_i^m + 1/\phi_s V_s^m)$, and is included to comply with classical Fickian diffusion for interface free, ideal mixtures.

2.2 Evaporation

The governing equations (Eqns. 1-3) do not account for the solvent evaporation during the fabrication of controlled release coatings. To capture the loss of solvent from the system during processing, we assume that evaporation occurs homogeneously across the evaporating surface. Thus, for a two-dimensional system with lateral dimension w and height h defined by $x \in (0,w)$, $y \in (0,h)$, evaporation occurs only along the $y = h$ surface. We note that this

surface is now a moving boundary, $h = h(t)$, and must satisfy $\nu(\phi_i^G - \phi_i^L) = V^s(J_i^G - J_i^L)$, where we have introduced superscripts to signify the the liquid and gas phases, ν is the velocity of the $y = h$ interface ($\nu = \partial h/\partial t$), and J_i are the molar fluxes for each species. Assuming the gas phase does not contain drug or polymer and only the solvent has a non-zero flux across the liquid/gas interface, we can sum the boundary condition over i and find $\nu(\phi_s^G - 1.0) = V^s J_s^G$. If we further assume that the solvent comprises a small fraction of the gas phase ($\phi_s^G \ll 1.0$), we can specify the dimensionless equation for the velocity of the evaporating surface as:

$$\widetilde{\frac{\partial h}{\partial t}} = -V^s J_s^G \frac{\lambda}{D^0}. \tag{8}$$

Once the interface velocity is known, we can designate the boundary conditions for ϕ_d and ϕ_p at the evaporating surface by dropping the superscripts for quantities in the liquid and recognizing that $\nu\phi_{i\neq s} = V^s J_{i\neq s}$, and therefore, $J_{i\neq s} = -J_s^G \phi_{i\neq s}$. To complete the model, we must specify the form of J_s^G. In reality, J_s^G will depend on a myriad of factors including: solvent partial pressure, solvent vapor pressure, temperature, air flow, and area of the evaporating surface. For simplicity, we assume that removal of solvent from the surface can be described by a first order mass transfer coefficient, k_e, with units length/time, and the average solvent composition at the surface, thus $V^s J_s^G = k_e \bar{\phi}_s|_{y=h}$. By solving Eqns. 1-3 simultaneously with Eqn. 8, we can now compute the evolution of microstructure in controlled release coatings during fabrication under varying evaporation conditions described by the mass transfer coefficient, k_e.

2.3 Material Parameters

Before conducting simulations, we must specify the unknown material quantities in the governing equations (Eqns. 1-3,8). In this manuscript, we have elected to apply thermodynamic and kinetic parameters that represent "characteristic" controlled drug release systems comprised of drug, polymer, and solvent. The material quantities are similar to those employed in previous work [9] and include the properties of the drug (d), polymer (p), processing solvent (s), and release solvent (r). The thermodynamic properties associated with the pure materials are summarized in Table 1. Note that the processing and release solvent were assumed to have the same pure material properties. The kinetic properties are given by $A_d = 5$ and $A_p = 15$, which implies the pure drug and pure polymer diffusivities are 10 and 1000 times slower, respectively, than the constant, characteristic diffusivity D^0 of the system when adequate solvent is present ($\phi_s > 0.20$). The final parameter associated with the pure materials is β, which was set to $0.001RT/V^s$. This value enables us to conduct computations based on the model equations in reasonable timeframes without changing the results in any significant way. In addition to the pure material properties, we must specify the parameters associated with interactions between the components, namely χ^k_{ij} and ϵ. For the amorphous components, the interaction parameters χ^a_{ij} were all set to zero, with the exception of $\chi^a_{dp} = 1.2$ and $\chi^a_{pr} = 6.0$. Similarly, the interactions between crystalline components χ^c_{ij} were all set to 2.5, except for $\chi^c_{dp} = 5.0$ and $\chi^c_{pr} = 10.0$. Finally, as in our previous work [9], we find that $\epsilon = 1.22 \times 10^{-6}\ J/cm$ provides a reasonable relationship between χ^k_{ij}, γ^k_{ij}, and δ^k_{ij}.

2.4 Simulations

To simulate processing and subsequent drug release, we start with a homogeneous, two-dimensional system with $w = 4\lambda$ and $h = 1.2\lambda$. We use a 400×100 mesh (initial dimensions equal to 0.010 λ and 0.012 λ for Δx and Δy, respectively) for the manufacturing simulations with $\lambda = 100nm$, *i.e.* 1 grid point = 1 nm. Further, the initial homogeneous composition is set to $\phi_d = 0.7\phi_d^0$, $\phi_p = 0.7(1 - \phi_d^0)$, and $\phi_s = 0.3$ where ϕ_d^0 is the bulk ratio of drug to total solids (drug + polymer) by volume, *i.e.* drug loading, and $\eta = 0$, everywhere. From this state, the system was evolved using a standard explicit finite difference scheme. A range of time steps were employed to optimize computation times with typical values between 6.4×10^{-7} λ^2/D^0 and 3.2×10^{-6} λ^2/D^0. Periodic boundary conditions were assumed for all fields at the boundaries defined by $x = 0$ and $x = w$ and a no flux condition was enforced at $y = 0$. No flux boundary conditions were also assumed at the evaporating surface ($y = h$) for the η field, while those for the composition fields were specified above.

Note that the height of the computational domain, specifically Δy at the evaporating interface, diminishes by $(k_e \bar{\phi_s}|_{y=h} \lambda/D^0)\widetilde{\Delta t}$ after each dimensionless time step, $\widetilde{\Delta t}$, in the finite difference scheme. To maintain equal mesh spacing in the y-direction, Δy, the interior grid positions are modified and the values of the field variables are interpolated at the new positions after each time step. We also introduced additional numerical noise during the processing simulations to simulate potential heterogeneous nucleation sites. While more sophisticated approaches have been developed (*e.g.* [25]), we simply add fluctuations to the η field during the processing simulations by introducing square regions of crystalline material ($\eta = 1.0$).

The square regions with dimensions $L \times L$ were generated randomly in space at a rate given by $N^0 \exp(-E(L)/kT)$, where k is Boltzmann's constant, N^0 is a frequency factor assumed to be $2.5 \times 10^{-5}\ \lambda^2/D^0$ and $E(L)$ is the energy associated with a perturbation of size L. Here, we model the perturbation energy as $(\Delta f L^3 - 6\gamma L^2)S$, with $\Delta f = (5 \times 10^4 kT)/(\lambda^3 S)$, and $\gamma = (100kT)/(\lambda^2 S)$.

The manufacturing simulation procedure was allowed to progress until $h = 0.9\lambda$, at which point the average solvent concentration was approximately 0.067. At this stage the structure is effectively kinetically locked, so to obtain essentially pure drug-polymer composites the remaining solvent is removed down to ≤ 0.01, and the mesh restructured such that $\Delta x = \Delta y$. In other words, the original 400×100 mesh is reduced to 400×90, and, again, the values of the field variables are interpolated at the new positions.

To simulate dissolution, the system is then placed in contact with the release media by adding an amorphous, solvent-rich area ($\phi_d = \phi_p = 0.025$) to the evaporating surface. The additional area is equivalent in size to the original composite; thus, the new system size is $4\lambda \times 1.8\lambda$. Finally, the system is allowed to evolve in contact with the new media, simulating structure evolution during release. For the release simulations, no-flux boundary conditions were assumed at all edges of the computational domain. Based on these calculations, the amount of drug released into the media can be determined as a function of time and the release profile can be specified for a particular system using the method described in the previous manuscript [8].

The methods described in the previous section were applied to probe the effect of both

evaporation rate and drug loading on the coating microstructure formed during manufacturing, as well as the impact of the microstructure on the subsequent release kinetics. To accomplish this, two series of manufacturing simulations were conducted. First, manufacturing simulations were conducted using different evaporation rate coefficients, k_e, over a range of $0.01D^0/\lambda$ to $0.63D^0/\lambda$ for a constant drug loading corresponding to $\phi_d^0 = 0.30$. The second series of manufacturing simulations aimed at probing the impact of drug loading were conducted by varying ϕ_d^0 between 0.14 and 0.50 at constant $k_e = 0.63D^0/\lambda$. To assess the variability in the calculations, each simulation condition was repeated three times with different seed values used to generate the numerical noise. After manufacturing, each computed composite microstructure was allowed to evolve in contact with the release media for 0.192 λ^2/D^0 and the release kinetics were characterized by generating a release profile.

3 Results

3.1 Evaporation Rate

During evaporation, regions near the evaporating surface become enriched in drug and polymer relative to the bulk of the system due to the depletion of solvent. This enrichment induces phase separation into two amorphous regions, one composed primarily of drug and the other primarily of polymer. Eventually, a third phase develops as some of the amorphous drug-rich regions begin to crystallize and grow. This is illustrated in Fig. 2, which depicts the evolution of both the composition and order parameter fields throughout the processing for a system with a drug loading, ϕ_d^0, equal to 0.30, and evaporation rate constant, k_e, equal to

0.01 D^0/λ. Fig. 2a shows the initial amorphous system with homogeneous composition. Note the left and right panels represent the composition and order parameter maps, respectively, and the dotted lines indicate the surface through which evaporation is occurring. In the composition map, the colors red, green and blue correspond to pure drug, polymer and solvent, respectively. Furthermore, in the order parameter map, blue corresponds to crystalline regions, while red corresponds to regions that are amorphous. As the simulation proceeds (Fig. 2b), the depletion of solvent at the evaporating surface results in phase separation into a layered structure comprised of drug-rich and polymer-rich layers, with the extent of separation decreasing with the distance from the evaporating surface. Note the perturbations in the order parameter field are a consequence of the noise introduced to induce heterogeneous nucleation. As the system continues to evolve, the amorphous, drug-rich layers break up into compact regions, a few of which crystallize, as shown in Fig. 2c. The nucleation of drug-rich crystals is favored where the drug concentration is high (*i.e.* near the evaporating surface) and at the substrate interface ($y = 0$), where the energy barrier for nucleation is reduced due to the imposition of a no-flux boundary condition (*i.e.* the crystals "wet" the substrate surface) [25]. As time progresses, more drug-rich crystals nucleate and grow at the expense of the amorphous drug (Fig. 2d and 2e), until the final microstructure is comprised entirely of crystalline, drug-rich particles, found primarily at the evaporating surface or substrate interface, contained within a nearly pure polymer matrix (Fig. 2f).

Changing the evaporation rate alone can have a significant impact on the microstructure that develops during processing of controlled release coatings. To illustrate this, we compare the results given in Fig. 2 with those provided in Fig. 3, which are based on the same simulation

conditions, except k_e has been increased from 0.010 D^0/λ to 0.630 D^0/λ (evaporation rate has been increased). Inspection of Fig. 3 reveals that while the morphology of the structural features and timeframe in which they evolve are similar in both cases, the onset of structure formation occurs after significantly more solvent has been removed when evaporation is more rapid. For example, complete phase separation into a layered structure near the evaporating surface is observed at roughly the same time in both cases ($\sim 0.006\lambda^2/D^0$) as illustrated in Fig. 2b and Fig. 3d. However, this phenomenon occurs at significantly different values for the average solvent concentration, $\bar{\phi}_s$, 0.26 and 0.18 for k_e equal to 0.010 D^0/λ and 0.630 D^0/λ, respectively. Similarly, we find compact drug-rich regions form and begin to crystallize after approximately 0.03 λ^2/D^0 in both cases (Fig. 2c and Fig 3e), while $\bar{\phi}_s$ is 55% lower (0.10 compared to 0.22) when $k_e = 0.630\ D^0/\lambda$. Thus, as the rate of solvent removal is increased, both the growth and crystallization of drug-rich regions are inhibited due to a reduction in the overall processing time, which is about a factor of eight faster for $k_e = 0.630 D^0/\lambda$ relative to $k_e = 0.010 D^0/\lambda$. Consequently, the final microstructure that develops can be quite different depending on evaporation rate, which is evident by comparing Fig. 2f and Fig. 3f. In Fig. 3f ($k_e = 0.630\ D^0/\lambda$), the drug-rich regions in the final microstructure are significantly smaller relative to those that formed under reduced evaporation rate conditions. Furthermore, when $k_e = 0.630\ D^0/\lambda$ a large fraction of these regions remain amorphous, whereas all of the phase separated drug is present in crystalline form for $k_e = 0.010\ D^0/\lambda$.

The results illustrated in Fig. 2 and Fig. 3 suggest that the final microstructure changes dramatically when k_e is varied from 0.010 D^0/λ to 0.630 D^0/λ. To throughly elucidate the impact of k_e on microstructure development, we can examine the final microstructures

that result from several values of k_e within this range, which are depicted in Fig. 4 for systems with $\phi_d^0 = 0.30$. As k_e is elevated from 0.010 D^0/λ (Fig. 4a) to 0.015 D^0/λ (Fig. 4b) no significant changes in microstructure are apparent. The structures in both cases are comprised of relatively large crystalline drug regions of uniform size within the polymer matrix. However, upon continued increase of k_e to 0.025 D^0/λ, disparities become evident. While the drug-rich regions remain completely crystalline, they become non-uniform in size and, on average, smaller, as shown in Fig. 4c. As k_e is raised further (*e.g.* Fig. 4d and 4e), these drug-rich regions are present in smaller sizes and greater number and are less likely to crystallize during processing. The results illustrated in Fig. 4 demonstrate that altering the time required to eliminate solvent from the system by a factor of two can have a significant impact on the development of microstructure in controlled release coatings. However, further modifications to k_e outside the range depicted resulted in no substantive differences. In fact, additional simulations conducted with different k_e values reveal that reducing k_e below 0.015 D^0/λ or raising k_e above 0.400 D^0/λ has no noticeable impact on the final microstructure. This suggests that for a particular system, the microstructure is only sensitive to evaporation over a finite range of k_e, which for the characteristic system considered here with $\phi_d^0 = 0.30$ is approximately 0.015 D^0/λ to 0.400 D^0/λ. Finally, note that over this transition, gradients in the structure occur along the height of the coating. Drug-rich regions near the surface are smaller and are more likely to crystallize than those in the bulk. As solvent is removed from the system, near-surface regions become depleted in solvent, which enhances the driving force and, thereby, the rate of crystallization, more rapidly than the bulk. Further, because the crystalline regions are more stable than those containing amorphous drug, they tend to coarsen at a much slower rate. Consequently, these regions persist as relatively small particles

until the majority of the solvent is removed through evaporation and the final microstructure is achieved. Because of the approximations made regarding loss of solvent during evaporation, our previous model was unable to capture the formation of these structural gradients, which can significantly impact drug release. Thus, the current model more accurately describes the evolution of microstructure during processing of controlled release coatings.

Because the kinetics of drug release are intrinsically linked to the distribution and state of drug within the coating (*i.e.* the microstructure), the changes in microstructure induced by varying k_e manifest as variations in the release profiles, which are illustrated in Fig 5. In the figure, the average drug release profile is provided for each value of k_e with error bars corresponding to plus/minus the standard deviation of three repetitions. The release profiles illustrate that as the evaporation rate is decreased and the microstructure is comprised of larger drug-rich regions, both the rate and extent of drug released increases, substantially in certain cases. For example, after being exposed to the release media for 0.032 λ^2/D^0, systems processed under conditions represented by $k_e = 0.01\ D^0/\lambda$ exhibited approximately a five-fold increase in the amount of drug released relative to systems corresponding to $k_e = 0.630\ D^0/\lambda$. Note that these large variations in release are restricted to about the first 0.064 λ^2/D^0 of release time, after which all of the profiles flatten out significantly. These observations reflect the fact that the large drug-rich regions at or near the surface of coatings fabricated under slower evaporation rates readily dissolve into the media and give rise to the steep initial slopes observed in the release profiles. After these regions are depleted, the release rates drop off significantly as the drug molecules now need to diffuse through the polymer matrix to reach the external media. When the evaporation rate is rapid, drug-rich regions at or near

the surface are relatively minute, which significantly reduces the amount of drug initially released. These results elucidate the substantial impact microstructure can have on release behavior, particularly the configuration at or near the coating surface. Again, the microstructure that develops in these near-surface regions is highly sensitive to evaporation conditions and evolves quite differently than in the bulk material, especially when the evaporation rate is relatively rapid. Therefore, the current model, which explicitly incorporates these effects, provides an improved framework to establish quantitative relationships between process, microstructure, and release behavior in these systems compared to the previous model, which did not distinguish between the surface and bulk regions of the coatings.

3.2 Drug Loading

The results presented above illustrate that for a particular drug loading ($\phi_d^0 = 0.30$) the near-surface structure, which has a significant impact on the rate and extent of drug release, can evolve much differently than in the bulk, especially at rapid evaporation rates. These differences between the structural configuration near the surface and in the bulk become more substantial as the drug loading is increased, as shown in Fig. 6 for the most rapid evaporation rate, $k_e = 0.630$. For example, Fig. 6a depicts a microstructure formed with a drug loading that corresponds to $\phi_d^0 = 0.14$. At this relatively low drug loading the driving force for phase separation and crystallization is insufficient for heterogeneities to form under rapid evaporation conditions, and the structure remains homogeneous throughout the coating thickness. For comparison, a coating microstructure manufactured with the same drug loading described in the previous section ($\phi_d^0 = 0.30$) is provided in Fig. 6b. As ϕ_d^0 is raised

further, we find that the surface structure becomes increasingly more distinct from the material in the bulk. When $\phi_d^0 = 0.42$ (Fig. 6c), plates of crystalline drug begin to form at the surface, while the bulk is comprised primarily of amorphous drug-rich regions with channel-like morphologies. Finally, Fig. 6d shows that nearly the entire surface becomes plated in crystalline drug at $\phi_d^0 = 0.50$ above a subsurface completely devoid of drug followed by interconnected amorphous regions in the bulk. Fig. 6 again illustrates that, at rapid evaporation rates, large variations in microstructure can develop through the thickness of the coating, especially at high drug loadings, which will ultimately impact drug release. These findings, which are consistent with coating microstructures observed in our laboratories, emphasize the impact of treating evaporation explicitly within the model.

To evaluate the ultimate impact on drug release, we also computed release profiles for the structures formed using varying drug loadings. The release profiles are summarized in Fig. 7, which provides the average drug release profile for each value of ϕ_d^0 with error bars again corresponding to plus/minus the standard deviation of three repetitions. As anticipated, increasing the drug loading increases the rate and extent of drug release. For example, the results demonstrate that drug release approximately doubled by increasing ϕ_d^0 from 0.14 to 0.30. The observation that release is approximately proportional to loading is consistent with the expected behavior for homogeneous systems [26]. However, as ϕ_d^0 is elevated above 0.30, large deviations from this ideal behavior are apparent. Most notably, increasing ϕ_d^0 from 0.30 to 0.50, an increase of only about 67%, resulted in a greater than six-fold increase in the amount of drug released after 0.032 λ^2/D^0. This behavior again reflects the significant increase in the concentration of drug-rich regions near the surface as ϕ_d^0 is raised above

0.30. As more drug accumulates near the surface during fabrication, where it can readily dissolve into the release media, we see a substantial increase in the amount of drug initially released into the media. Also, note that the variations in release are relatively small when ϕ_d^0 is very small (0.14) or very large (0.50). This observation is a consequence of the relatively homogeneous microstructures that form when ϕ_d^0 is small (Fig. 6a) and structures that exhibit a nearly complete drug-rich layer at the coating surface when ϕ_d^0 is large (Fig. 6d). Finally, we note that modifying the evaporation rate can have an impact on drug release that is comparable to altering the drug loading by a factor of two or more. This implies that the impact of evaporation conditions during fabrication can be as critical to performance as the amount of drug within the coating.

4 Discussion

In this manuscript, we have extended our previous model for microstructure evolution in controlled release coatings to explicitly incorporate the evaporation of the solvent during manufacturing. This modification, which captures potential structural gradients that may develop due to inhomogeneous solvent evaporation, enables us to more accurately capture the microstructure that forms during the fabrication of controlled release coatings. For example, by assuming that $D^0 = 4 \times 10^{-12} cm^2/s$ and $\lambda = 5 \times 10^{-4} cm$, which are reasonable for the systems of interest, we can scale our simulations to the length and time scales associated with the experimental structures shown in Figure 1. Under these assumptions the amount of time required to remove the solvent from $\bar{\phi}_s = 0.30$ to $\bar{\phi}_s = 0.067$, ranges from 0.63 to

5.4 h for $\phi_d^0 = 0.30$. The time required for solvent removal over a comparable range in the experiments (30 % w/w drug) was approximately 1.5 and 5.0 h. for the conditions denoted as "fast" and "slow" evaporation, respectively. Upon inspection of the experimental structures shown in Figure 1 and the predicted structures in Figure 3, we find that the structure formed under "slow" evaporation conditions depicted in Figure 1c closely resembles the predicted microstructure in Figure 3a. Note that under the scaling introduced above, the solvent removal times are comparable, 5.4 h. for the simulation and 5.0 h. in the experiment. Further, we find that the predicted structure in Figure 3d is comparable to the experimental structure formed under "fast" evaporation conditions in Figure 1d. Again, the corresponding solvent removal times are similar, 1.4 h. for the simulation and 1.5 h. in the experiment. Thus, the predicted microstructures are consistent to those observed experimentally with similar drug loadings and evaporation rates. We note that under this scaling the interfacial thicknesses and energies, as well as the order parameter mobility, become unrealistically large, although the relative values of the interface energies and, therefore, the equilibrium contact angles (*i.e.* geometry) remain the same. So, even though some material quantities become unphysical, the scaled predictions compare quite well to experimental data. Finally, while the previous model provided drug release predictions that were consistent with those found in the literature [7], initial tests in our laboratories suggest that the drug release behavior of the structures predicted by incorporating evaporation explicitly in the model more accurately captures the release behavior in actual systems than the previous model.

The simulations described in this manuscript indicate that both drug loading and evaporation rate can have a profound influence on the microstructure and subsequent release kinetics

of controlled drug release coatings. However, these predictions are only applicable to systems with chemistries similar to those of the of the representative system considered here. Most notably, because we assumed the polymer to be relatively insoluble in the release medium, these predictions would not reflect of the behavior of systems containing polymers that readily dissolve along with the drug during release. In fact, predictions based on our previous model suggest that systems containing polymers that dissolve into the release medium are more sensitive to the underlying manufacturing variables. The previous model could not, however, capture the proclivity for the formation of large plates of drug-rich crystals to form preferentially at or near the surface of the coating. The implication of this new insight is the potential release of large crystalline drug particulates from the coating if the surrounding polymer degrades prior to the dissolution of these large drug crystals. These "degradable" polymer systems are currently of particular interest because, in a response to a recent hypothesis based on epidemiological analyses that suggested the presence of the polymer coating leads to an increased risk of late-term myocardial infarction and, potentially, death, a recent trend in the DES industry is to incorporate polymers that will completely dissolve *in-vivo* [27]. Thus, the results described in this manuscript suggest that, in addition to a potential increased variability in the release kinetics, the impact of undissolved drug crystals possibly being liberated from the coating on clinical outcomes must be assessed to ensure the safety and effcacy of this new class of DES systems.

In the development and application of the model, a few simplifying assumptions were made. For example, while the model does explicitly incorporate evaporation, it assumes that loss of solvent occurs evenly across the evaporating surface such that, at a given time, the coating

will be the same thickness everywhere. However, in actual systems we expect local perturbations in evaporation rate as regions near the surface become non-uniformly enriched or depleted in solvent. Because of this restriction, the current model is also unable to capture edge effects, or the impact of uneven solution application, that may arise due to certain casting procedures and/or substrate geometry. While it is analytically straightforward to remove the restriction of uniform evaporation, it would add significant complexity to the model. Further, we expect the impact of these effects on the microstructure and subsequent release kinetics will be minimal, and substantial insight into the behavior of these systems can be obtained using the current model. In addition, calculations were initiated from a state with a solvent concentration corresponding to $\phi_s = 0.30$. During the fabrication of actual controlled release coatings, however, the solution of dissolved drug and polymer is initially much more dilute, typically $\phi_s \geq 0.95$. However, additional simulations demonstrate that, for our choice of material parameters, increasing the initial solvent concentration above 0.30 had no substantive impact on the final microstructure that evolves. Thus, to avoid prohibitively long computation times, we started the manufacturing calculations with relatively concentrated solutions.

Finally, we note that the simulations described in this manuscript assumed that the controlled release coatings were manufactured by solution casting. In other words, the final coating is a result of a single application of the mixture of dissolved drug and polymer. However, in some commercial applications, controlled release coatings are manufactured by spray coating, where the mixture is sprayed upon the substrate creating a very thin layer of drug and polymer. By passing the spray source over the substrate repeatedly, the layers ac-

cumulate and, eventually, the final coating thickness is obtained. Although the mechanisms of manufacturing are more complex in this scenario, the same algorithms described in this manuscript can be applied to gain insight into the impact of process variables, such as the raster speed and number of passes made by the spray source, on the microstructure of the final coating. For example, the effect of raster speed can be assessed by repeatedly adding thin layers of dissolved material to the surface at varying, predetermined rates until the desired thickness is obtained. While the current framework does not allow individual spray droplets to be modeled, it should be possible to further modify the theory to incorporate coatings with variable thickness as discussed above. However, employing the simplified approach described here would yield substantial insight into the impact of process variables on coating microstructure using spray methods and allow comparisons between the two methods, spray coating and solution casting, to be made.

5 Summary

We have extended our previous diffuse interface model for microstructure development during the manufacturing of controlled drug release coatings to explicitly incorporate solvent removal by evaporation. Solvent removal is implemented through the introduction of a unique boundary condition that allows the essential physics of evaporation to be captured with a mass transfer coefficient without requiring a complete physico-chemical description of the system constituents in the gas phase. Using this relatively straightforward approach, we have probed the influence of both evaporation rate and drug loading on the microstructure

that develops during coating fabrication and the impact of that microstructure on the drug release kinetics for a characteristic system consisting of drug, polymer, and solvent. We find that by including evaporation, the predicted structures are inhomogeneous through the coating thickness, which is consistent with experimental observations and not captured by the previous model. For the system considered here, evaporation rate was observed to have a significant impact on the configuration of the final microstructure, but only over a finite range. Further, these changes in microstructure strongly influence the subsequent release kinetics, resulting in up to a five-fold change in the amount of drug released. By varying the drug loading, we also found that the final microstructures exhibited surface structures that became increasingly more distinct from the material in the bulk as the relative amount of drug in the coating was increased. At the highest drug loadings ($\phi_d^0 = 0.50$), nearly the entire surface became plated with crystalline drug above a subsurface completely devoid of drug. The formation of these plate-like structures resulted in a substantial increase in the rate and extent of drug released as ϕ_d^0 is elevated from 0.30 to 0.50. By scaling the simulations to the typical length and time scales of coating fabrication conducted in our laboratories, we find that predicted impact of evaporation rate on microstructure for our characteristic system is consistent with the experimental observations. We also note that the concentration of crystalline drug particles at the surface of the coating may have clinical implications not previously considered, particular in systems containing biodegradable polymers. Finally, the methodologies outlined in this manuscript are not limited to coatings fabricated by solution casting. In fact, the same algorithms described here should be applicable to gain insight into the impact of process variables for other coating manufacturing methods.

Disclaimer

The mention of commercial products, their source, or their use in connection with the material reported herein is not to be construed as either an actual or implied endorsement of the US Food and Drug Administration or the National Institute of Standards and Technology.

References

[1] P. Lemos, P. Surruys, J. Sousa, Drug-eluting stents, Circulation 107 (2003) 3003–7.

[2] D. Faxon, Bringing reality to drug-eluting stents, Circulation 109 (2004) 104–42.

[3] C. Wright, The rise and rise of stents, Scrip Magazine (2006) 10–13.

[4] R. Bawa, R. Siegel, B. Marasca, M. Karel, R. Langer, An explanation for the controlled release of macromolecules from polymers, J. Control. Release 1 (1985) 259–67.

[5] S. Ranade, K. Miller, R. Richard, A. Chan, M. Allen, M. Helmus, Physical characterization of controlled release of paclitaxel from the taxus^{TM}express2^{TM}drug-eluting stent, Journal of Biomedical Materials Research Part A 71A[4] (2004) 625–34.

[6] K. Wormuth, D. DeWitt, G. Haugstad, Characterization of drug eluting coatings on medical devices, Polymer Preprints 46 [2] (2005) 1222.

[7] K. Kamath, J. Barry, K. Miller, The taxus^{TM}drug-eluting stent: A new paradigm in controlled drug delivery, Advanced Drug Delivery Reviews 58 (2006) 412–36.

[8] D. Saylor, C.-S. Kim, D. Patwardhan, J. Warren, Diffuse-interface theory for structure formation and release behavior in controlled drug release systems, Acta Biomater. 3 (2007) 851–64.

[9] D. Saylor, C.-S. Kim, D. Patwardhan, J. Warren, Modeling microstructure development and release kinetics in controlled drug release coatings, J. Pharm. Sci.

[10] J. Cahn, J. Hilliard, Free energy of nonuniform systems. i. interfacial free energy, J. Chem. Phys. 28 (1958) 258–67.

[11] J. Cahn, On spinodal decomposition, Acta. Metall. 9 (1961) 795–801.

[12] S. Allen, J. Cahn, A microscopic theory of domain wall motion and its experimental verification in fe-al alloy domain growth kinetics, J. Phys. 38 (1977) C7–C51.

[13] M. Grassi, G. Grassi, Mathematical modelling and controlled drug delivery: Matrix systems, Current Drug Delivery 2 (2005) 97–116.

[14] T. Higuchi, Rate of release of medicaments from ointment bases containing drugs in suspension., J Pharm Sci. 50 (1961) 874–75.

[15] P. Ritger, N. Peppas, A simple equation for description of solute release i. fickian and non-fickian release from non-swellable devices in the form of slabs, spheres, cylinders or discs, J. Control. Release 5 (1987) 37–42.

[16] R. Langer, N. Peppas, Chemical and physical structure of polymers as carriers for controlled release of bioactive agents - a review, Rev. Macromol. Chem. Phys. C23 (1983) 61–126.

[17] R. Siegel, J. Kost, R. Langer, Mechanistic studies of macromolecular drug release from macroporous polymers. i. experiments and preliminary theory concerning completeness of drug release, J. Control. Release 8 (1989) 223–36.

[18] R. Siegel, R. Langer, Mechanistic studies of macromolecular drug release from macroporous polymers. ii. models for the slow kinetics of drug release, J. Control. Release 14 (1990) 153–67.

[19] A. Karma, W.-J. Rappel, Phase-field model of dendritic sidebranching with thermal noise, Phys. Rev. E 60 [4] (1999) 3614–25.

[20] P. Flory, Thermodynamics of high polymer solutions, J. Chem. Phys. 9 (8) (1941) 660.

[21] M. Huggins, Solution of long chain compounds, J. Chem. Phys. 9 (5) (1941) 440.

[22] J. Vrentas, J. Duda, Diffusion in polymer-solvent systems. ii. a predictive theory for the dependence of diffusion coefficients on temperature, concentration, and molecular weight, J. Polym. Sci., Polym. Phys. Ed. 15 (1977) 417–39.

[23] J. Duda, Y. Ni, J. Vrentas, An equation relating self-diffusion and mutual diffusion coefficients in polymer-solvent systems, Macromolecules 12 [3] (1979) 459–62.

[24] J. Zielinski, J. Duda, Predicting polymer/solvent diffusion coefficients using free-volume theory, AIChE J. 38 [3] (1992) 405–15.

[25] L. Granasy, T. Pusztai, D. Saylor, J. Warren, Phase-field theory of heterogeneous crystal nucleation, Phys. Rev. Lett. 98 (3) (2007) 035703.

[26] P. Shewman, Diffusion in Solids, The Minerals, Metals, and Materials Society, Warrendale, PA, 1989.

[27] E. Camenzind, P. Steg, W. Wijns, Stent thrombosis late after implantation of first-generation drug-eluting stents: A cause for concern, Circulation 115 (2007) 1440–55.

Table 1: Properties of the pure components

	drug	polymer	solvent
$L(J/cm^3)$	100	100	100
$T_m(K)$	388	268	208
$V(cm^3/mol)$	400	4000	100
$\gamma^{od}(mJ/m^2)$	29.3	20.2	15.7
$\delta^{od}(nm)$	0.7	0.7	0.7

Figure Captions

Figure 1: Three-dimensional confocal microscopy data illustrating the tetracycline distribution in styrene-isobutylene-styrene (SIBS) co-polymer manufactured by solution casting. Solutions were made by dissolving a mixture of 30 % by weight tetracycline and the balance SIBS in tetrahydrofuran (THF). The solutions were then cast onto glass substrates and the solvent was allowed to evaporate in a controlled environment under conditions that either inhibited or promoted evaporation. Isosurfaces that enclose regions with a high relative tetracycline concentration are shown in (a) and (b) for inhibited and promoted evaporation, respectively. Although compact, drug-rich particles form throughout the coating thickness when solvent evaporation is comparatively rapid (b), relatively large particles are observed near the surface of the coating while particles within the coating appear to have two different characteristic sizes, especially near the glass substrate, one comparable to the near-surface particles and one much finer. As solvent evaporation is inhibited (a), the drug-enriched regions become coarser, approximately one-half of the entire coating thickness, and more uniform in size. Also included in the figure are plots of the relative tetracycline concentration along typical two-dimensional slices through the coating thickness for both the inhibited (c) and promoted (d) evaporation conditions. The dotted lines shown in (c) and (d) indicate the surfaces through which evaporation of the solvent occurs.

Figure 2: Simulation results illustrating the development of microstructure during coating fabrication for a system with $\phi_d^0 = 0.30$ and an evaporation rate coefficient of $k_e = 0.01 D^0/\lambda$. The evolution of the composition fields and the order parameter field are depicted in left and

right column of images, respectively. The rows in the figure represent the configuration of the fields after the following process times, t_p, in units of λ^2/D^0 with the average remaining solvent concentration, $\bar{\phi}_s$, given in parentheses: (a) 0.000 (0.30), (b) 0.0064 (0.26), (c) 0.032 (0.22), (d) 0.0480 (0.18), (e) 0.192 (0.10), and (f) 0.304 (0.067). A key is provided for both field maps. In the composition map, the colors red, green, and blue correspond to pure drug, polymer, and solvent, respectively. Further, in the order map, blue corresponds to a perfectly crystalline regions, while red corresponds to regions that are completely amorphous. The dotted lines shown in (a)–(f) indicate the surfaces through which evaporation of the solvent occurs.

Figure 3: Simulation results illustrating the development of microstructure during coating fabrication for a system with $\phi_d^0 = 0.30$ and an evaporation rate coefficient of $k_e = 0.63D^0/\lambda$. The evolution of the composition fields and the order parameter field are depicted in left and right column of images, respectively. The rows in the figure represent the configuration of the fields after the following process times, t_p, in units of λ^2/D^0 with the average remaining solvent concentration, $\bar{\phi}_s$, given in parentheses: (a) 0.000 (0.30), (b) 0.0010 (0.26), (c) 0.0042 (0.22), (d) 0.0066 (0.18), (e) 0.0254 (0.10), and (f) 0.0382 (0.067). A key is provided for both field maps. In the composition map, the colors red, green, and blue correspond to pure drug, polymer, and solvent, respectively. Further, in the order map, blue corresponds to a perfectly crystalline regions, while red corresponds to regions that are completely amorphous. The dotted lines shown in (a)–(f) indicate the surfaces through which evaporation of the solvent occurs.

Figure 4: Images illustrating the effect of solvent evaporation rate on the microstructure that forms during the manufacturing of a characteristic controlled drug release coating with $\phi_d^0 = 0.30$. The rows in the figure represent microstructures that formed under conditions that correspond to the following evaporation rate coefficients, k_e, with units of D^0/λ and process times, t_p, with units of λ^2/D^0 in parentheses: (a) 0.010 (0.312), (b) 0.015 (0.202), (c) 0.025 (0.138), (d) 0.063 (0.0794), and (e) 0.63 (0.038). The left and right columns of images correspond to the composition fields and the order parameter field, respectively. A key is provided for both field maps. In the composition map, the colors red, green, and blue correspond to pure drug, polymer, and solvent, respectively. Further, in the order map, blue corresponds to a perfectly crystalline regions, while red corresponds to regions that are completely amorphous. The dotted lines shown in (a)–(e) indicate the surfaces through which evaporation of the solvent occurred.

Figure 5: Calculated drug release profiles for systems with $\phi_d^0 = 0.30$. The lines in the plot correspond to the mean amount of drug released from three repetitions as a function of time for microstructures formed under conditions corresponding to a range of evaporation rate coefficients, k_e, from 0.01 to 0.63 D^0/λ. The error bars correspond to $\pm$ one standard deviation ($n = 3$) about the mean.

Figure 6: Images illustrating the effect of drug loading, ϕ_d^0, on the microstructure that forms

during the manufacturing of a characteristic controlled drug release coating under conditions that correspond to an evaporation rate coefficient, k_e, of 0.63 D^0/λ. The rows in the figure represent microstructures that formed in systems with ϕ_d^0 equal to (a) 0.14, (b) 0.30, (c) 0.42, and (d) 0.50. The left and right columns of images correspond to the composition fields and the order parameter field, respectively. A key is provided for both field maps. In the composition map, the colors red, green, and blue correspond to pure drug, polymer, and solvent, respectively. Further, in the order map, blue corresponds to a perfectly crystalline regions, while red corresponds to regions that are completely amorphous. The dotted lines shown in (a)–(d) indicate the surface through which evaporation of the solvent occurred.

Figure 7: Calculated drug release profiles for systems manufactured under conditions that correspond to an evaporation rate coefficient, k_e, of 0.63 D^0/λ. The lines in the plot correspond to the mean amount of drug released from three repetitions as a function of time for microstructures in systems with drug loadings, ϕ_d^0, of 0.14 (black), 0.30 (red), 0.42 (green), and 0.50 (blue). The error bars correspond to $\pm$ one standard deviation ($n = 3$) about the mean.

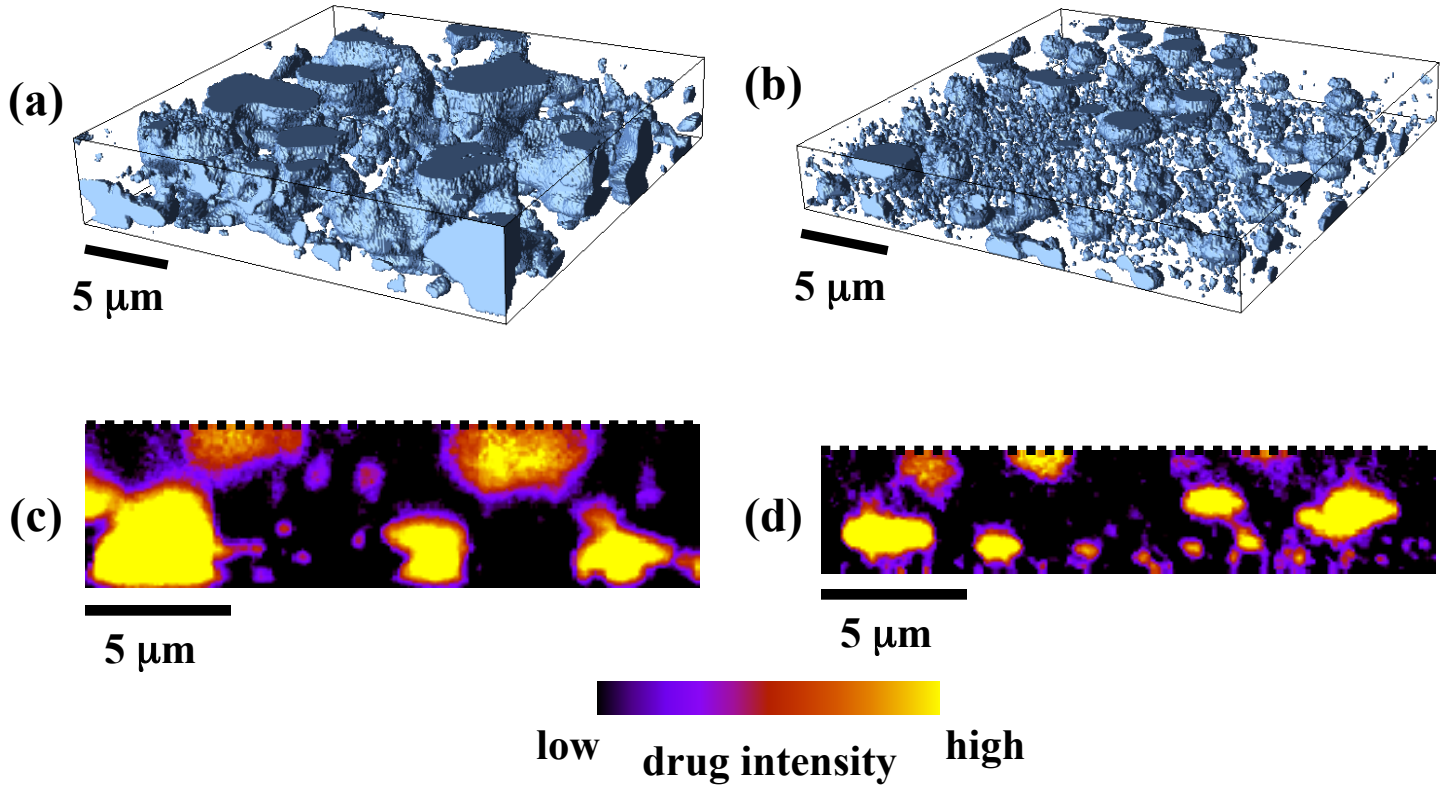

Fig. 1 Three-dimensional confocal microscopy data illustrating the tetracycline distribution in styrene-isobutylene-styrene (SIBS) co-polymer manufactured by solution casting. Solutions were made by dissolving a mixture of 30 % by weight tetracycline and the balance SIBS in tetrahydrofuran (THF). The solutions were then cast onto glass substrates and the solvent was allowed to evaporate in a controlled environment under conditions that either inhibited or promoted evaporation. Isosurfaces that enclose regions with a high relative tetracycline concentration are shown in (a) and (b) for inhibited and promoted evaporation, respectively. Although compact, drug-rich particles form throughout the coating thickness when solvent evaporation is comparatively rapid (b), relatively large particles are observed near the surface of the coating while particles within the coating appear to have two different characteristic sizes, especially near the glass substrate, one comparable to the near-surface particles and one much finer. As solvent evaporation is inhibited (a), the drug-enriched regions become coarser, approximately one-half of the entire coating thickness, and more uniform in size. Also included in the figure are plots of the relative tetracycline concentration along typical two-dimensional slices through the coating thickness for both the inhibited (c) and promoted (d) evaporation conditions. The dotted lines shown in (c) and (d) indicate the surfaces through which evaporation of the solvent occurs.

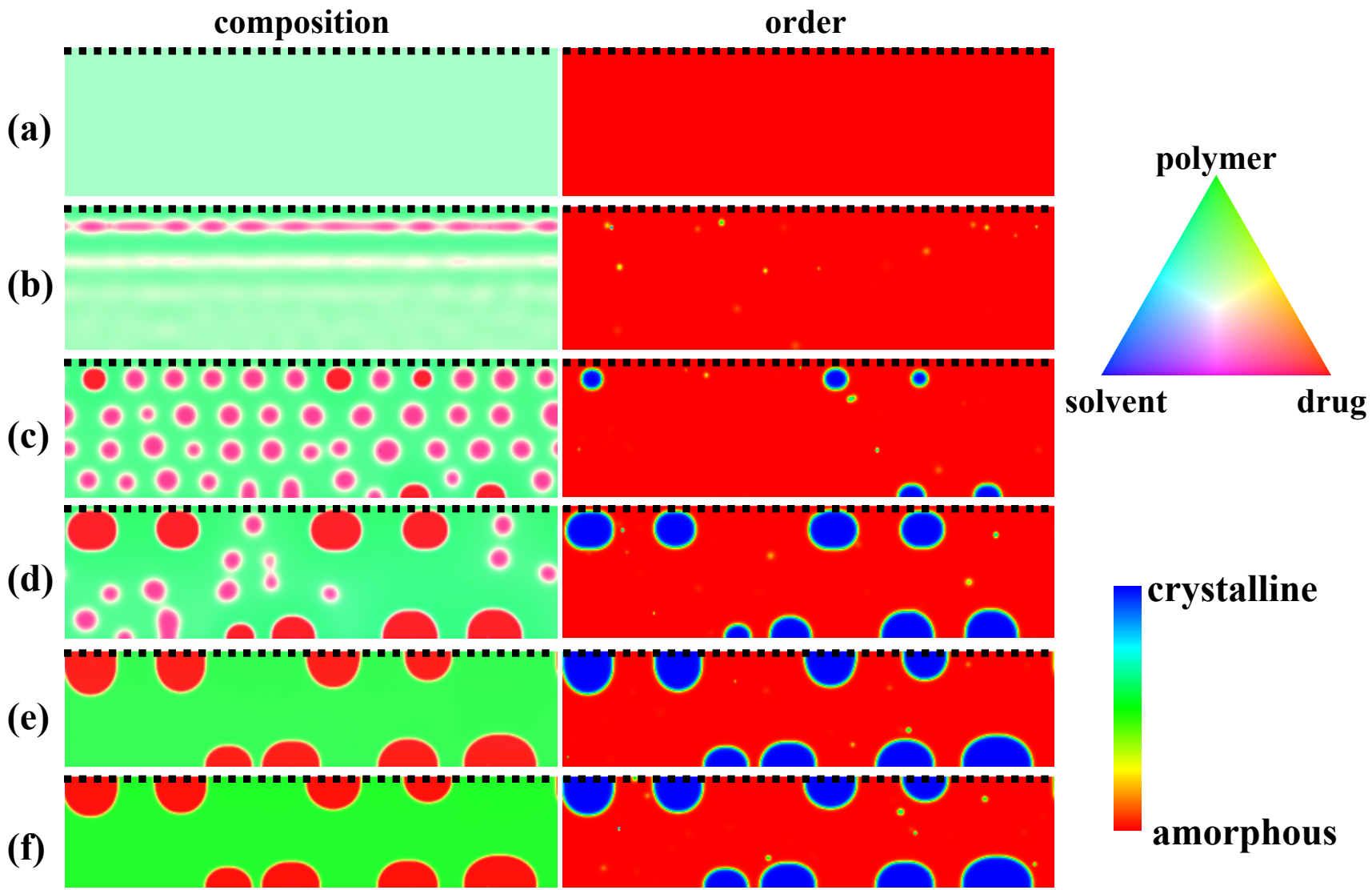

Fig.2 Simulation results illustrating the development of microstructure during coating fabrication for a system with ϕ_d^0 = 0.30 and an evaporation rate coefficient of k_e = 0.01 D^0/λ. The evolution of the composition fields and the order parameter field are depicted in left and right column of images, respectively. The rows in the figure represent the configuration of the fields after the following process times, t_p, in units of λ^2/D^0 with the average remaining solvent concentration, $\bar{\phi}_s$, given in parentheses: (a) 0.000 (0.30), (b) 0.0064 (0.26), (c) 0.032 (0.22), (d) 0.0480 (0.18), (e) 0.192 (0.10), and (f) 0.304 (0.067). A key is provided for both field maps. In the composition map, the colors red, green, and blue correspond to pure drug, polymer, and solvent, respectively. Further, in the order map, blue corresponds to a perfectly crystalline regions, while red corresponds to regions that are completely amorphous. The dotted lines shown in (a)-(f) indicate the surfaces through which evaporation of the solvent occurs.

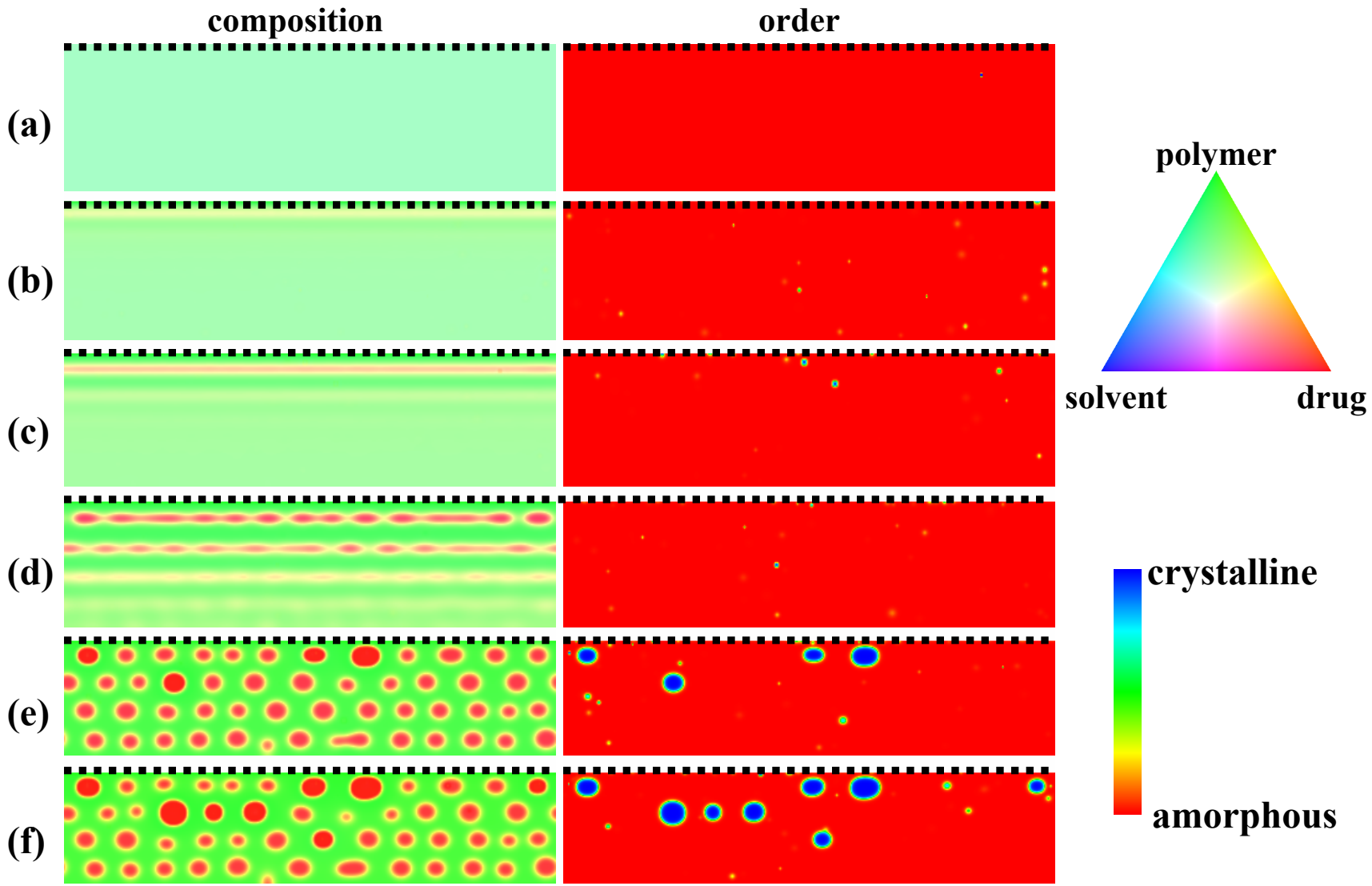

Fig.3 Simulation results illustrating the development of microstructure during coating fabrication for a system with ϕ_d^0 = 0.30 and an evaporation rate coefficient of k_e = 0.63 D^0/λ. The evolution of the composition fields and the order parameter field are depicted in left and right column of images, respectively. The rows in the figure represent the configuration of the fields after the following process times, t_p, in units of λ^2/D^0 with the average remaining solvent concentration, $\bar{\phi}_s$, given in parentheses: (a) 0.000 (0.30), (b) 0.0064 (0.26), (c) 0.032 (0.22), (d) 0.0480 (0.18), (e) 0.192 (0.10), and (f) 0.304 (0.067). A key is provided for both field maps. In the composition map, the colors red, green, and blue correspond to pure drug, polymer, and solvent, respectively. Further, in the order map, blue corresponds to a perfectly crystalline regions, while red corresponds to regions that are completely amorphous. The dotted lines shown in (a)-(f) indicate the surfaces through which evaporation of the solvent occurs.

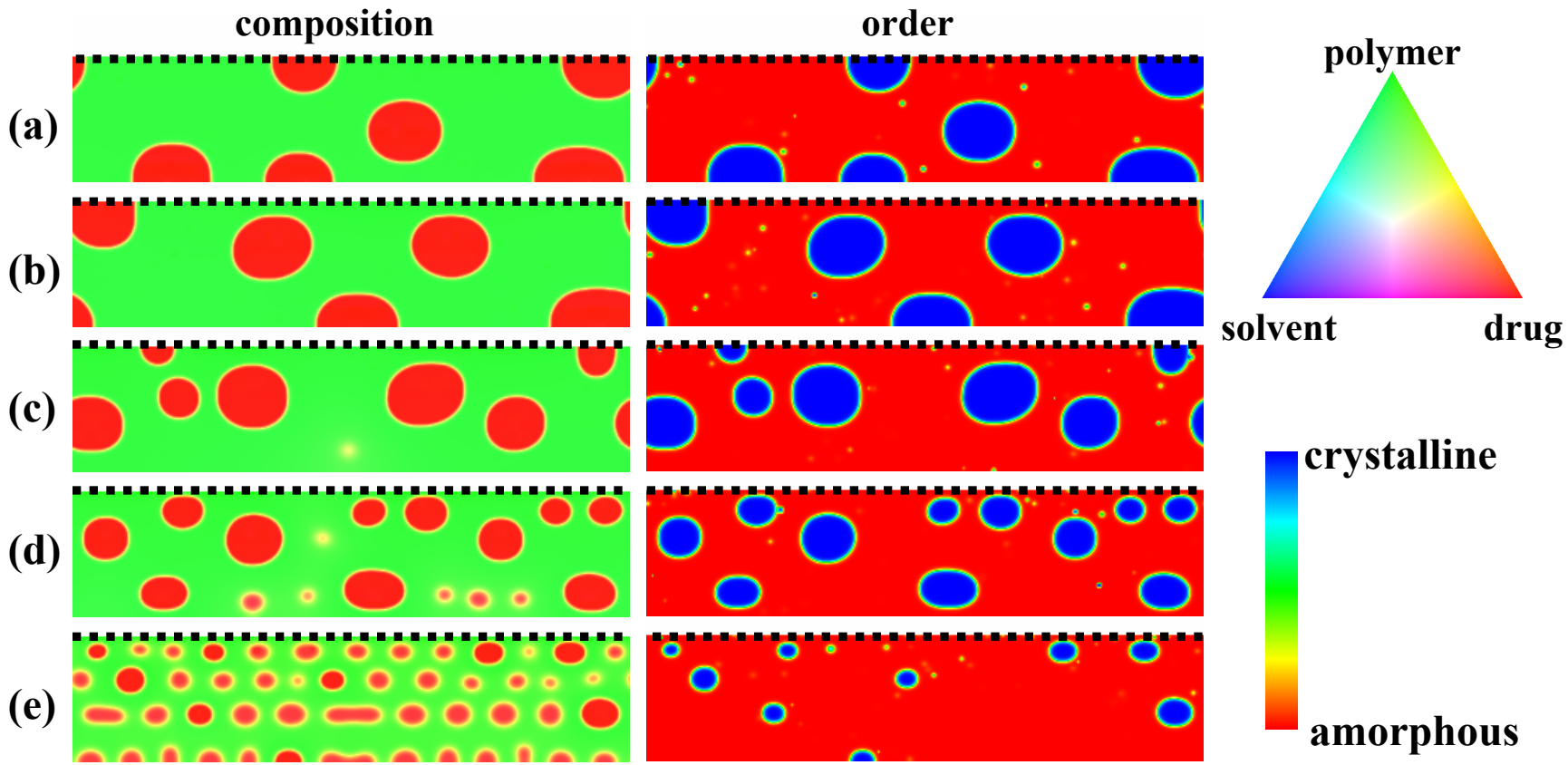

Fig.4 Images illustrating the effect of solvent evaporation rate on the microstructure that forms during the manufacturing of a characteristic controlled drug release coating with $\phi_d^0 = 0.30$. The rows in the figure represent microstructures that formed under conditions that correspond to the following evaporation rate coefficients, k_e, with units of D^0/λ and process times, t_p, with units of λ^2/D^0 in parentheses: (a) 0.010 (0.312), (b) 0.015 (0.202), (c) 0.025 (0.138), (d) 0.063 (0.0794), and (e) 0.63 (0.038). The left and right columns of images correspond to the composition fields and the order parameter field, respectively. A key is provided for both field maps. In the composition map, the colors red, green, and blue correspond to pure drug, polymer, and solvent, respectively. Further, in the order map, blue corresponds to a perfectly crystalline regions, while red corresponds to regions that are completely amorphous. The dotted lines shown in (a)-(e) indicate the surfaces through which evaporation of the solvent occurred.

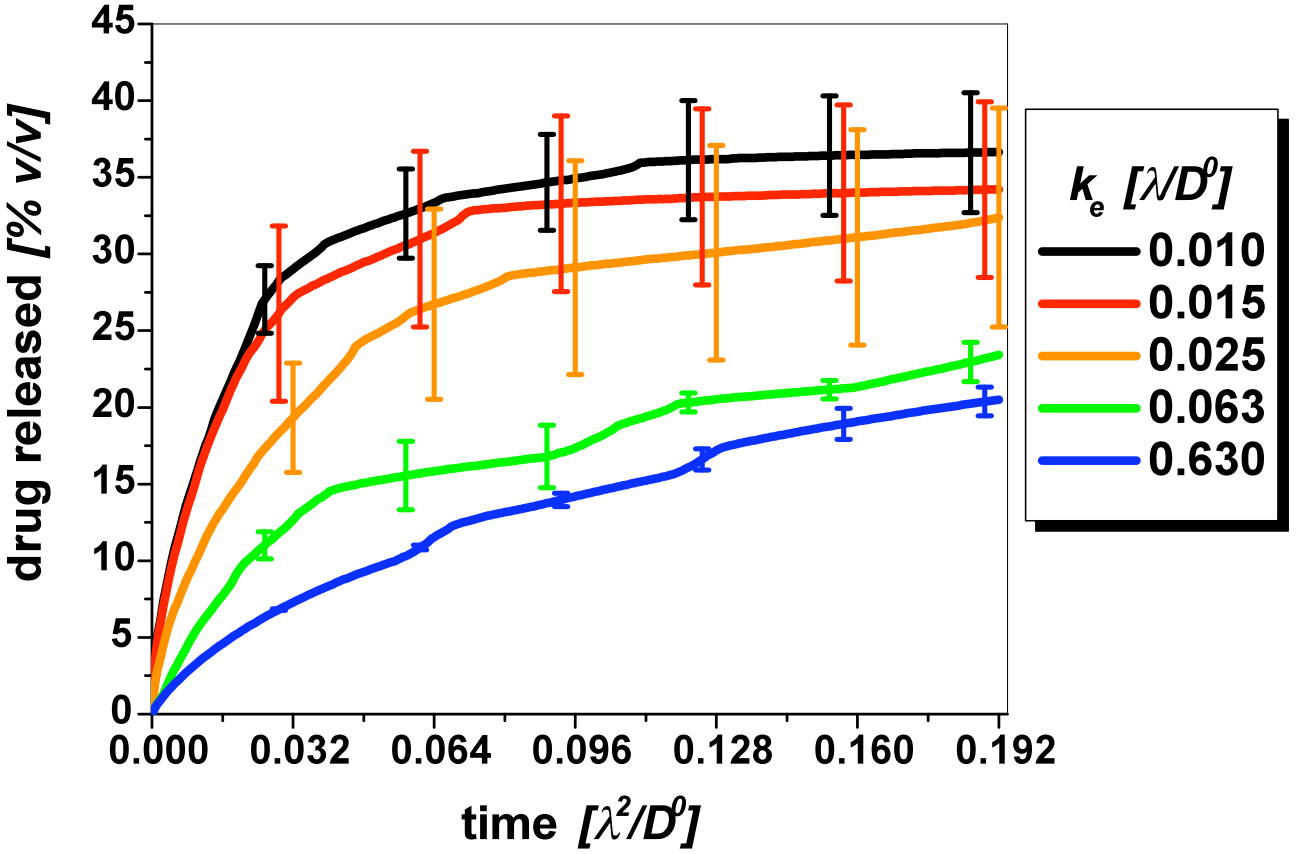

Fig.5 Calculated drug release profiles for systems with $\phi_d^0 = 0.30$. The lines in the plot correspond to the mean amount of drug released from three repetitions as a function of time for microstructures formed under conditions corresponding to a range of evaporation rate coefficients, k_e, from 0.01 to 0.63 D^0/λ. The error bars correspond to ± one standard deviation (n=3) about the mean.

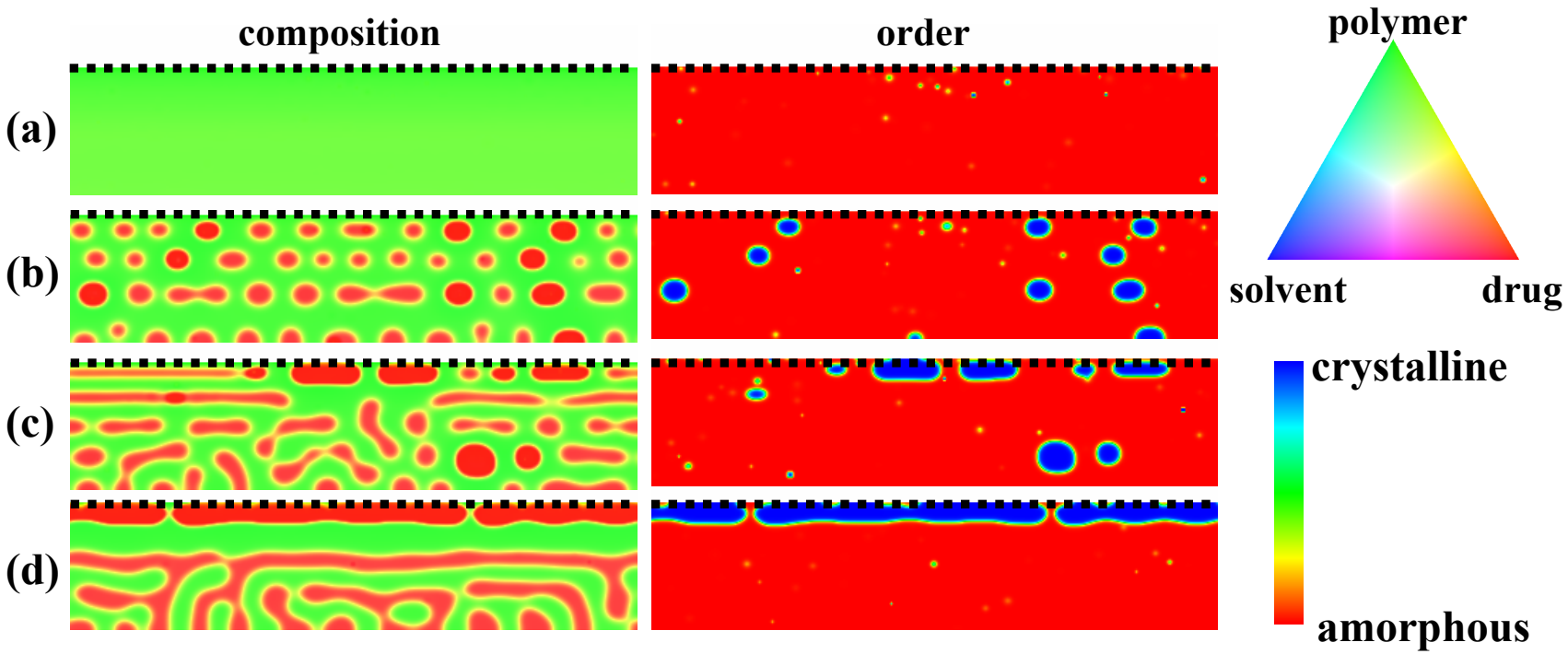

Fig. 6 Images illustrating the effect of drug loading, ϕ_d^0, on the microstructure that forms during the manufacturing of a characteristic controlled drug release coating under conditions that correspond to an evaporation rate coefficient, k_e, of 0.63 $D^0\backslash\lambda$. The rows in the figure represent microstructures that formed in systems with fd0 equal to (a) 0.14, (b) 0.30, (c) 0.42, and (d) 0.50. The left and right columns of images correspond to the composition fields and the order parameter field, respectively. A key is provided for both field maps. In the composition map, the colors red, green, and blue correspond to pure drug, polymer, and solvent, respectively. Further, in the order map, blue corresponds to a perfectly crystalline regions, while red corresponds to regions that are completely amorphous. The dotted lines shown in (a)-(d) indicate the surfaces through which evaporation of the solvent occurred.

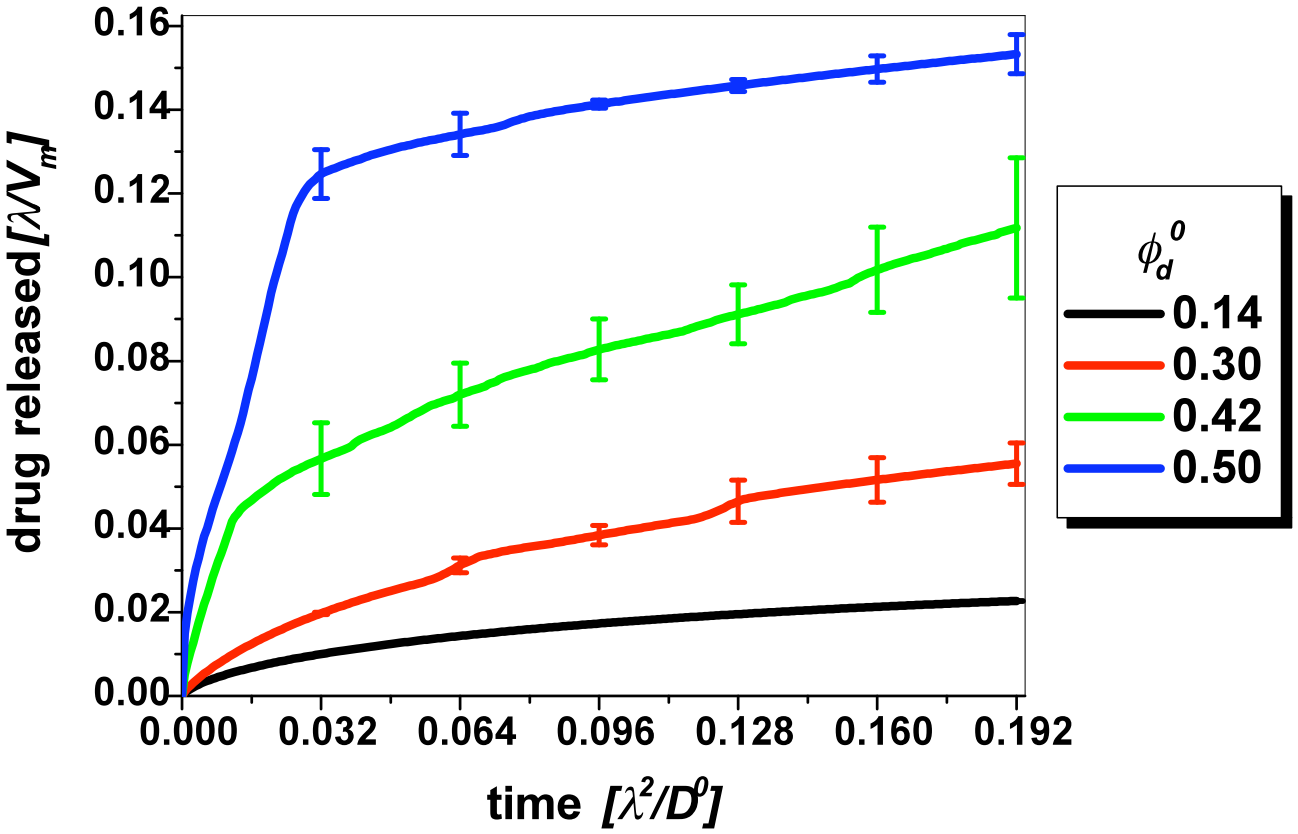

Fig. 7 Calculated drug release profiles for systems manufactured under conditions that correspond to an evaporation rate coefficient, k_e, of 0.63 D^0/λ. The lines in the plot correspond to the mean amount of drug released from three repetitions as a function of time for microstructures in systems with drug loadings, ϕ_d^0, of 0.14 (black), 0.30 (red), 0.42 (green), and 0.50 (blue). The error bars correspond to ± one standard deviation (n=3) about the mean.